Analysis of Plasma-Tail Motions for Comets C/2001 Q4 (NEAT) and C/2002 T7 (LINEAR) Using Observations from SMEI

Buffington, A.; Bisi, M. M.; Clover, J. M.; Hick, P. P.; Jackson, B. V.; Kuchar, T. A.

Published in:
Astrophysical Journal

DOI:
10.1086/529039

Publication date:
2008

Citation for published version (APA):
Buffington, A., Bisi, M. M., Clover, J. M., Hick, P. P., Jackson, B. V., & Kuchar, T. A. (2008). Analysis of Plasma-Tail Motions for Comets C/2001 Q4 (NEAT) and C/2002 T7 (LINEAR) Using Observations from SMEI. *Astrophysical Journal*, *677*(1), 798-807. https://doi.org/10.1086/529039

The Astrophysical Journal, 677:798–807, 2008 April 10

ANALYSIS OF PLASMA-TAIL MOTIONS FOR COMETS C/2001 Q4 (NEAT) AND C/2002 T7 (LINEAR) USING OBSERVATIONS FROM SMEI

A. Buffington,[1] M. M. Bisi,[1] J. M. Clover,[1] P. P. Hick,[1] B. V. Jackson,[1] and T. A. Kuchar[2]

Received 2007 October 23; accepted 2007 December 17

ABSTRACT

Comets C/2001 Q4 (NEAT) and C/2002 T7 (LINEAR) passed within ~0.3 AU of Earth in April and May of 2004. Their tails were observed by the Earth-orbiting Solar Mass Ejection Imager (SMEI) during this period. A time series of photometric SMEI sky maps displays the motions and frequent disruptions of the comet plasma tails. Ephemerides are used to unfold the observing geometry; the tails are often seen to extend ~0.5 AU from the comet nuclei. Having selected 12 of the more prominent motions as "events" for further study, we introduce a new method for determining solar wind radial velocities from these SMEI observations. We find little correlation between these and the changing solar wind parameters as measured close to Earth, or with coarse three-dimensional reconstructions using interplanetary scintillation data. A likely explanation is that the transverse sizes of the solar wind perturbations responsible for these disruptions are small, $\lesssim$0.05 AU. We determine the radial velocities of these events during the disruptions, using a technique only possible when the observed comet tails extend over a significant fraction of an AU. We find typical radial velocities during these events of 50–100 km s^{-1} lower than before or afterward. Time durations of such events vary, typically from 3 to 8 hr, and correspond to comet traversal distances ~10^6 km (0.007 AU). We conclude that these large disturbances are primarily due to ubiquitous solar wind flow variations, of which these measured events are a subset.

Subject headings: comets: individual (C/2001 Q4 (NEAT), C/2002 T7 (LINEAR), C/2004 F4 (Bradfield)) — solar wind — Sun: coronal mass ejections (CMEs)

Online material: mpeg animations

1. INTRODUCTION

For over half a century, comet plasma (type I) tails have been recognized as naturally occurring probes of the solar wind, useful for providing information about not only its mean global properties, but also its spatial and temporal variations (e.g., Biermann 1951, 1957; Brandt & Chapman 2004; Mendis 2006, and references therein). The plasma tail, while immersed in the solar wind and lying in the comet's orbital plane, is not pointed radially away from the Sun, but lags behind the radial by an aberration angle (in the sense opposite to the comet's motion) of typically about 5° (Brandt & Chapman 2004, and references therein). When the comet encounters a sudden variation of the solar wind dynamics, a "kink" or bend in the tail can appear when some of the comet's apparent motion is perpendicular to the comet tail. In this case the aberration angle changes, and the resulting bend propagates with time down the tail. This kink can also appear as a brightening of the comet tail when the line of sight has a significant component within the orbital plane. Finally, when a comet tail spans the heliospheric current sheet (HCS), a "disconnection event" can occur, with the trailing end of the tail completely separating from the main tail structure (Niedner & Brandt 1978; Brandt & Snow 2000).

These variations are of particular interest for this work, which presents new comet-tail measurements of data from a space-borne instrument, the Solar Mass Ejection Imager (SMEI), (Eyles et al. 2003; Jackson et al. 2004) in Earth orbit on board the Air Force *Coriolis* satellite. In particular, three comets were observed by SMEI in 2004 April and May: C/2001 Q4 (NEAT), C/2002 T7 (LINEAR), and C/2004 F4 (Bradfield). Both NEAT and LINEAR passed close by Earth, within ~0.3 AU. At times their plasma tails can be seen extending up to 8×10^7 km (~0.5 AU), and they exhibit considerable variability in both position and brightness. On the other hand, comet Bradfield passed less close to Earth and at high ecliptic latitude; its tail remained quiescent throughout the observation period.

An earlier publication (Kuchar et al. 2007) highlights six of the larger tail "disruptions" for comets NEAT and LINEAR, derived from the same SMEI observations. That article notes that one disruption coincides with the nearby passage of a coronal mass ejection (CME). Two of the five remaining events cannot be explained by a passage of the comet tail through the HCS. The present work examines the data in much greater detail. We find that comet tails during this time period are in almost continuous motion; we here identify 12 of the largest tail-motion "events" (some individual and some multiple) for further study.

The instrumentation from which data were obtained is described in § 2; § 3 describes the analysis of the data and comparison of other data with these SMEI observations. Section 4 presents the results, and § 5 a summary and our conclusions.

2. INSTRUMENTATION: THE SOLAR MASS EJECTION IMAGER

SMEI was designed to detect and forecast the arrival of CMEs and other heliospheric structures moving toward and passing by Earth; it consists of three CCD cameras, each viewing a 60° × 3° band of sky oriented roughly perpendicular to the satellite's velocity vector. The *Coriolis* satellite circles Earth in a roughly polar orbit at an altitude of 840 km. In each 102 minute orbit, the fields of view of the combined cameras sweep over almost the entire sky. The cameras' sensitivity covers the optical wave band

[1] Center for Astrophysics and Space Sciences, University of California at San Diego, La Jolla, CA 92093–0424; abuffington@ucsd.edu, mmbisi@ucsd.edu , jclover@ucsd.edu, pphick@ucsd.edu, bvjackson@ucsd.edu.

[2] Institute for Scientific Research Boston College Chestnut Hill, MA 02147; kuchar@bc.edu.

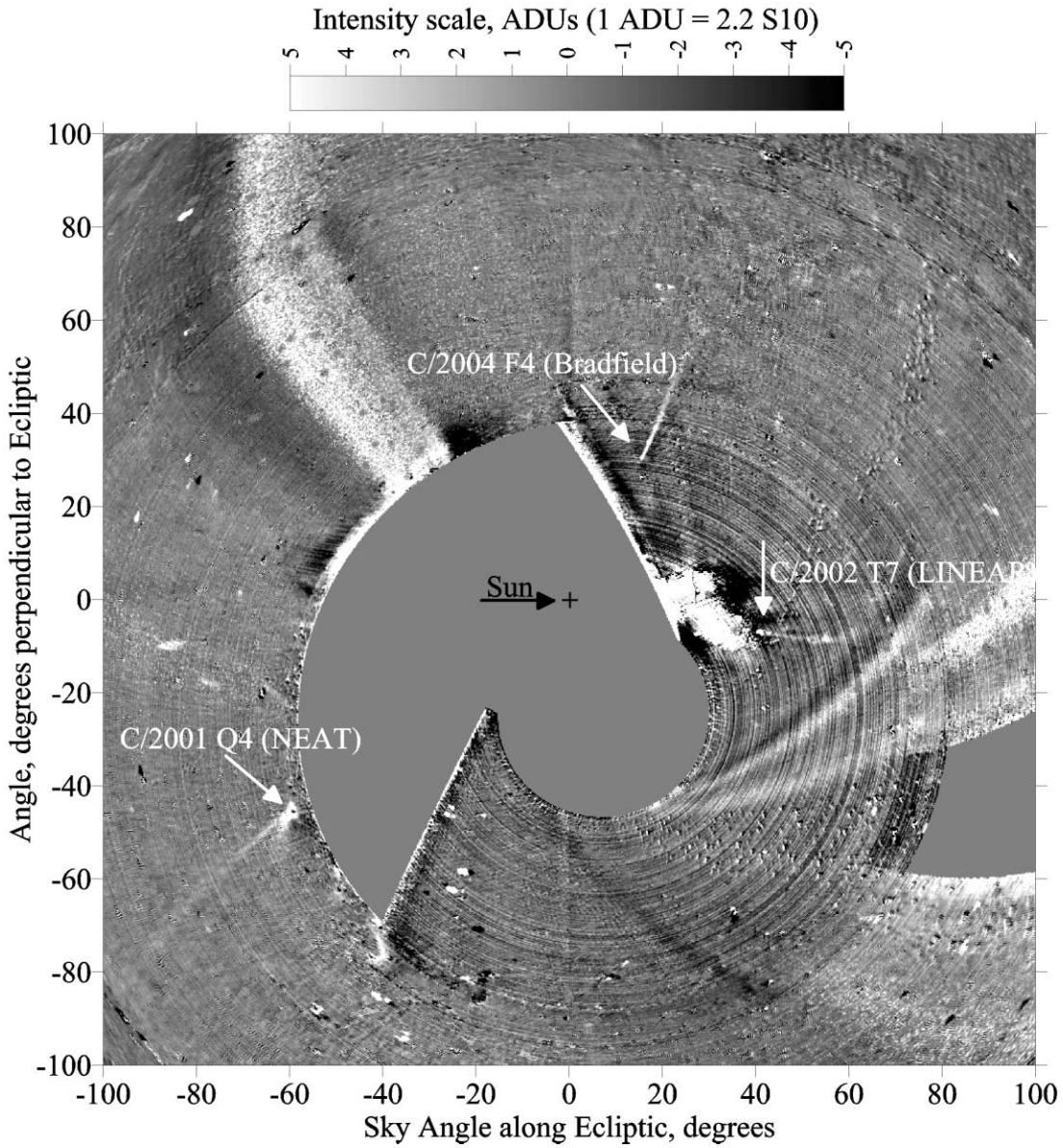

FIG. 1.— Equal-radius fisheye sky map in Sun-centered ecliptic coordinates for an orbit starting at 11:48 UT on 2004 May 7. North is up. In this projection, radial angles are mapped linearly from the Sun (*black cross*), and angles around the Sun are preserved over the entire radial distance. The white arrows indicate the locations of the three comets. Separate plasma and short dust tails are visible for comets NEAT and LINEAR. Blank spaces in the map include a circular exclusion zone never viewed by SMEI (below center), an adjoining arc where the shutter for the camera viewing nearest the Sun was closed (left center), and an area excluded due to contamination from the nearby Moon (lower right). Some auroral light contamination is visible to the upper left. An mpeg animation is available in the online *Journal*.

(0.4–1.1 μm), and the sky angular resolution is about 0.5°. Differential photometric precision is about 0.1% over most of the sky, but degrades near bright stars or the Moon, during periods of bright aurora (Mizuno et al. 2005), or when auroral electrons or South Atlantic Anomaly (SAA) protons impact the CCD (Buffington et al. 2006). The SMEI instrument is fully described by Eyles et al. (2003), and the SMEI mission and data analyses by Jackson et al. (2004).

3. DATA ANALYSIS

SMEI data for a single orbit consist of ~1500 single CCD frames for each camera. These are normalized and stitched together into a single sky map by the primary SMEI data analysis process (Jackson et al. 2004; Hick et al. 2005). Average stellar and zodiacal-light contributions and a slowly varying 10 day average response are then subtracted. Stars brighter than 6th magnitude are individually subtracted (Hick et al. 2007). The resulting maps provide a photometric measure of surface brightness versus angular position in the sky. A time series of these maps clearly displays the comet-tail motions and disruptions. However, angular measurements using these sky maps may prove inconvenient for quantitative analysis, since the comet nucleus moves and is at a variable distance. Thus, the actual linear perturbation sizes depend on the distance and orientation of the comets relative to the observer. The next two sections describe making the sky maps into movies and further processing of these movies to display the comet-tail motions with the comet nucleus held fixed, and finally with the effects of changing distance and perspective removed.

3.1. *Comet Movies*

Figure 1 shows a sky map with the three comets indicated. The coordinate frame is ecliptic; the projection is of an equal-angle

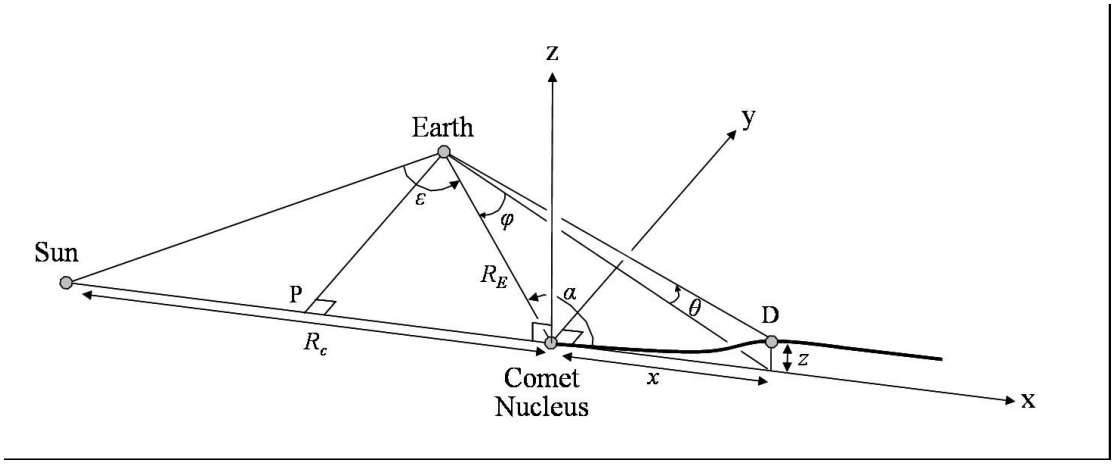

FIG. 2.—Comet coordinate frame; the nucleus is at the origin. The x-axis connects the Sun and the nucleus as shown, with positive pointing away from the Sun. Point "P" is the location where the x-axis is closest to Earth. The x-z plane is perpendicular to the line connecting P and Earth. In this coordinate frame the comet tail remains close to the positive x-axis. Locations in the sky near the comet, such as point "D", as seen from Earth, are specified by the two angles (ϕ, θ), where ϕ is the spherical coordinate "longitude" of the given point along the comet's tail, positive away from the Sun, and θ its "latitude." For the observations presented here, point P is usually (but not always) located as shown between the Sun and comet nucleus on the negative x-axis. Note that this coordinate frame follows the motion of the comet nucleus relative to the Sun and Earth.

fisheye centered on the Sun out to a square of $\pm 100^\circ$. The intensity scale is the SMEI analog-to-digital units (ADUs), which relate as shown at the top of Figure 1 to "S10's", the equivalent intensity of a 10th magnitude star spread over a $1^\circ \times 1^\circ$ sky bin (see § 13.3 in Cox 2000 and, for the surface brightness conversion scale, Buffington et al. 2007). This map covers more than a hemisphere of sky.

A sequence of 539 sky maps like Figure 1 is assembled into a movie in which the evolving motion of the comets is clearly visible. The time period starts at 24 April 2004, 05:27 UT, extends through 2 June 2004 and covers 564 SMEI orbits.[3] This movie shows considerable tail activity throughout this time period for both NEAT and LINEAR, but only smooth, featureless motion for Bradfield, which fades from view well before the end of the movie.

Figure 2 shows another coordinate frame that is useful to present and analyze the comet observations. This analysis uses comet ephemerides from the Minor Planet and Comet Ephemeris Service[4] to place the comet nucleus at the origin of a standard coordinate frame and orient the coordinate frame's x-axis along the line to the Sun.

Figure 3 shows a single frame from a movie of comet LINEAR using the angles (ϕ, θ) introduced in Figure 2. The comet tails span a considerable angle in the sky, occasionally greater than 90° when Figure 2's point P lies within the comet's tail, farther from the Sun than the comet nucleus. Since the comet tails are nearly straight, extending in three-dimensional (3D) space approximately along the positive x-axis, the apparent angular

[3] This and the other comet-tail movies described are available as mpeg animations in the electronic edition of the *Journal*, and can also be viewed at http://smei.ucsd.edu/comets/.

[4] See http://www.cfa.harvard.edu/iau/MPEph/MPEph.html.

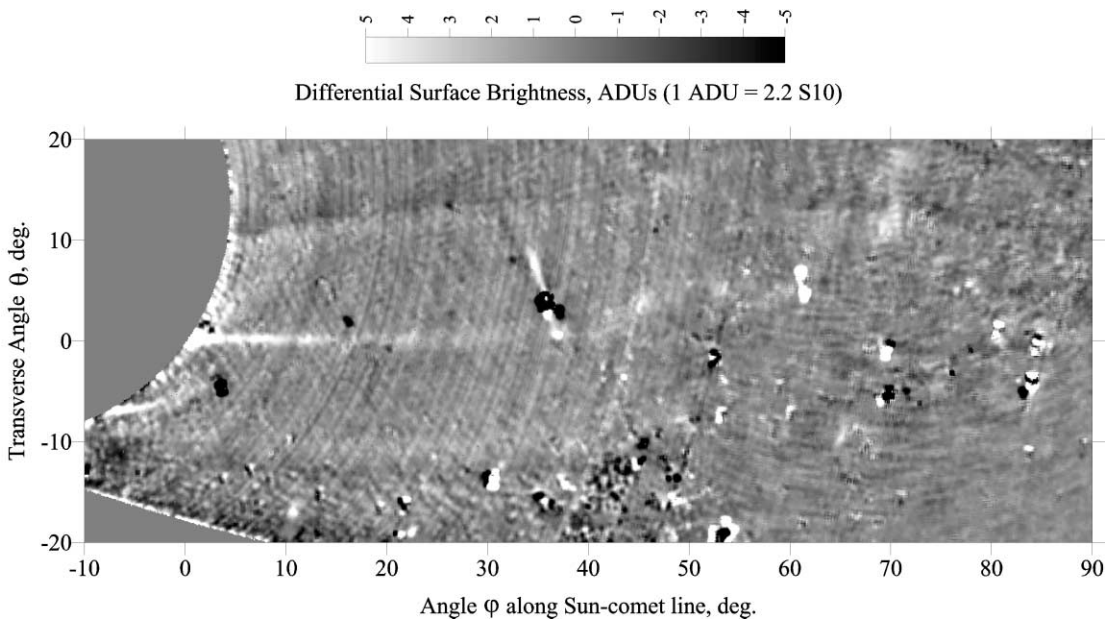

FIG. 3.—View of the tail of comet LINEAR for the orbit starting at 02:54 UT on 2004 May 20. This represents a single frame in the comet movie. Here the comet nucleus is located at the origin, displaced as shown from the left-hand axis. Horizontal and vertical axes represent the angles (ϕ, θ) of Fig. 2.

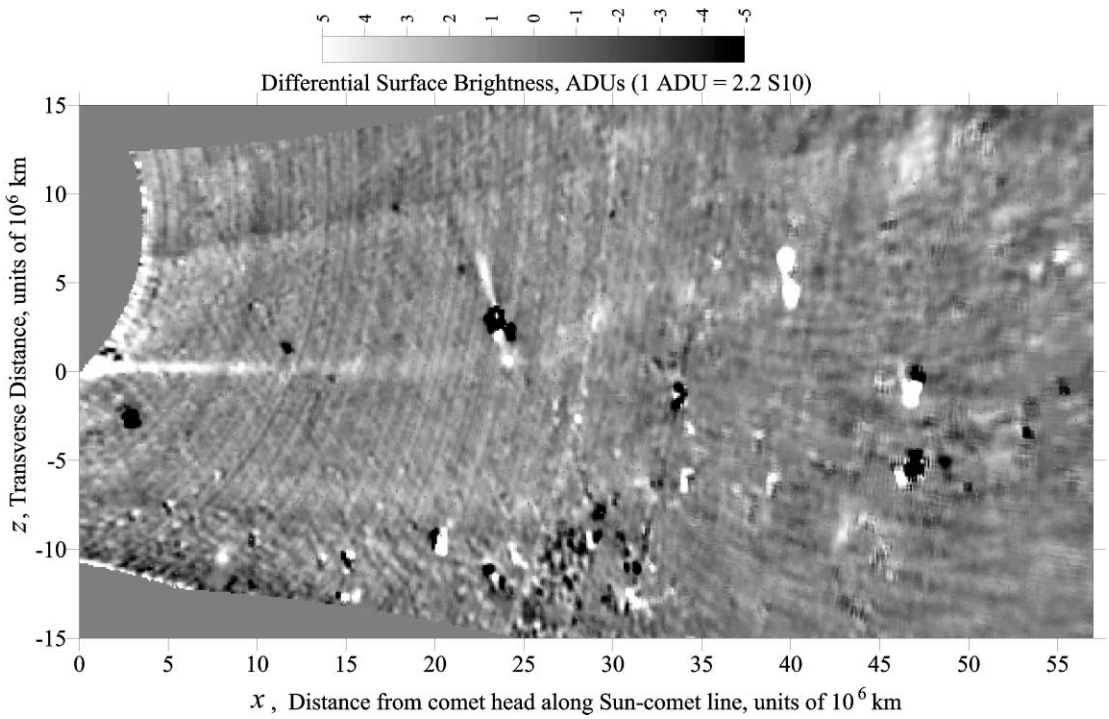

FIG. 4.—Same as Fig. 3, but with the perspective corrected and transformed into units of 10^6 km as illustrated in Fig. 2. Here x is from eq. (2) and z from eq. (3).

extent of a comet tail is limited to less than 90° as measured from point P (at 90° a point would be infinitely far away from the observer). The next section describes the conversion from Figure 2's angular values (ϕ, θ), to the linear (x, z).

3.2. *Unfolding the Perspective*

The angular location (ϕ, θ) of a given point along the comet tail can be converted to (x, z), where x is the 3D linear distance down the comet tail along the Sun-comet line, and z the distance perpendicular to this and to the line from point P to Earth. First, ephemeris values are found for the Sun-comet distance R_c, the comet-Earth distance R_E, and the elongation of the Sun-comet angle as viewed from Earth, ε.

Next, let α be the angle between the x-axis and the comet-to-Earth line. Then,

$$\alpha = \varepsilon + \arcsin(R_E \sin\varepsilon / R_c), \quad (1)$$

for given values of (ϕ, θ),

$$x = R_E \cos\alpha [1 - \tan\alpha / \tan(\alpha + \phi)], \quad (2)$$

and finally,

$$z = x \tan\theta (\sin\alpha / \sin\phi). \quad (3)$$

Figure 4 shows Figure 3, but with the resulting perspective-corrected linear (x, z) values. Movies 2–5 show both NEAT (Movies 2 and 3) and LINEAR (Movies 4 and 5) individual comet-tail motions for the entire period without (Movies 2 and 4) and with (Movies 3 and 5) the perspective corrected. Bradfield is shown only without the perspective corrected in Movie 6, since little is gained from perspective-correcting its tail, which remained quiescent during the observation.

3.3. *A Qualitative Description of the Comet Movies*

The fisheye movie centered on the Sun (as the selected frame in Fig. 1) is the best choice to view all three comets at once throughout the period studied in this article. Numerous CMEs are also visible in this movie as areas of faintly enhanced brightness sweeping across the sky, although only one (see Kuchar et al. 2006, 2007) occurs in close proximity to comet-tail activity. Individual comet movies are more suitable for viewing the changing topography of their tail features. Movies of comets C/2001 Q4 (NEAT) and C/2002 T7 (LINEAR) both exhibit considerable tail activity, while the tail of comet C/2004 F4 (Bradfield) remains straight and unstructured until it fades from view. In addition to the plasma tails, shorter dust tails are also visible during portions of the movies for NEAT and LINEAR.

The plasma-tail motions seen for both of these comets are a combination of (1) a continuous "waving" like a wind-blown smoky trail of a torch being carried; (2) a wave or kink appearing close behind the nucleus and propagating down the tail; and (3) one or more bright knots propagating down the tail, usually connected by a fainter trail.

Typically, a kink at first appears as an abrupt change. In the majority of cases an increase in aberration angle relative to the unperturbed comet tail is seen, and this angle often increases further as the disturbance propagates down the tail. In this case the material trailing the kink appears to be catching up with the material within and ahead of the kink. Various unrelated artifacts are also visible in the movies, especially in the wide-angle fisheye Sun-centered ecliptic movie (Movie 1).[5] In most cases these artifacts and empty places in the sky do not interfere much with viewing and measuring the comet-tail motions.

[5] Most notable of these are the aurorae (Mizuno et al. 2005), twice daily periodic interference of the SAA (rapidly changing spotty broad arcs, a residue of the particle contamination removal), passage of the bright Moon (empty sections of sky with bright or noisy edges), and a population of variable stars that were not removed by the star-subtraction procedure (periodically flashing spots). In addition, the sky is left blank where no data are recorded, within about 20° of the Sun, and out to even larger elongations where the shutter was closed for the camera viewing closest to the Sun, to prevent direct sunlight from entering the inner optics chamber.

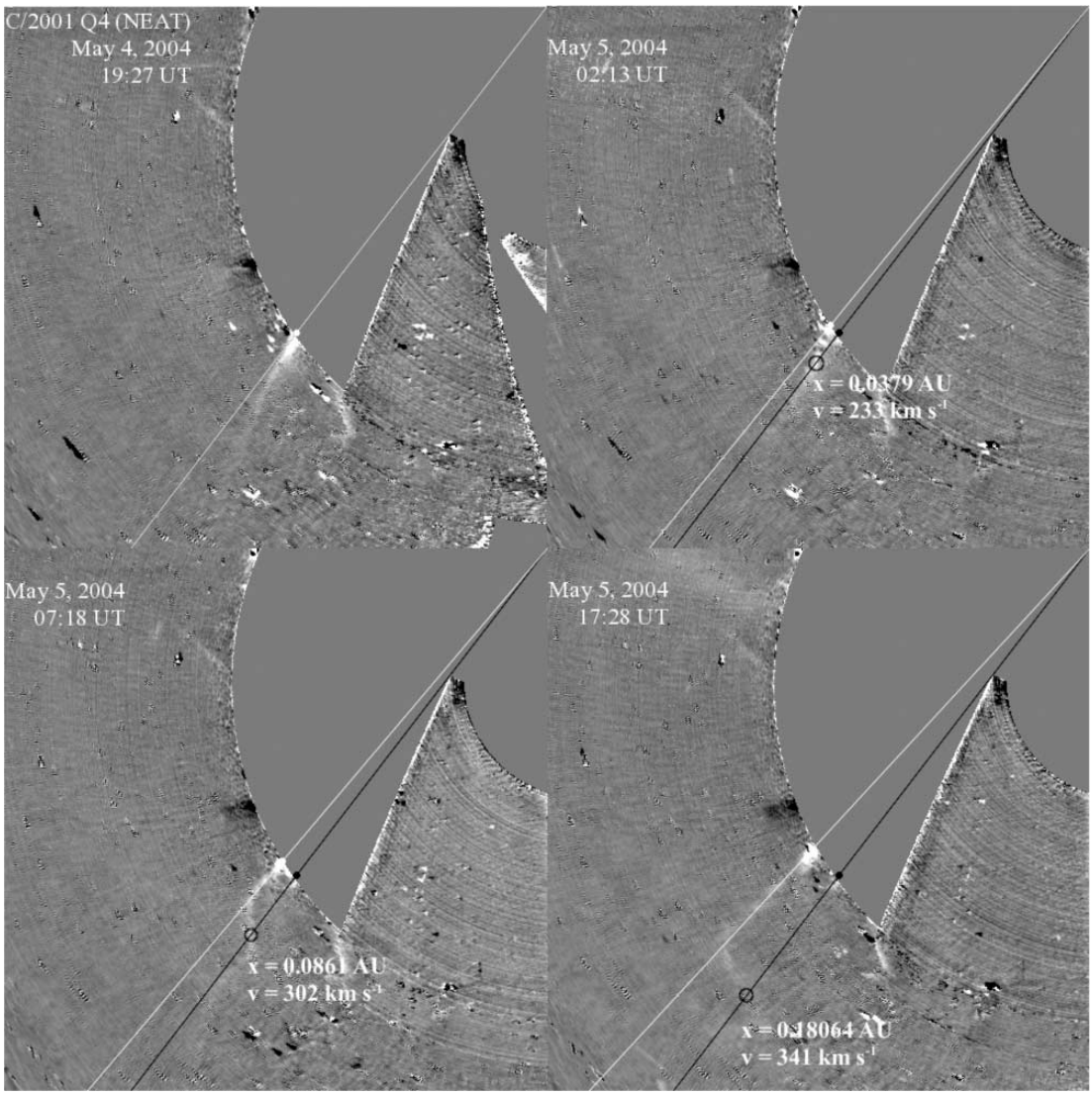

FIG. 5.—Four sections extracted from separate Sun-centered fisheye sky maps. The Sun is located in the top right corner of each frame, and a white line is plotted from the Sun to the comet's nucleus for each frame. This line plotted along the Sun-comet line for the first frame is kept fixed as a black line in subsequent frames, and is used as the reference point for radial velocity measurements; a new white line is plotted along the Sun-comet line of the current (new) frame. Intersection of the comet tail with the black line is indicated by a circle. The radial velocity values here are determined by the angle between this circle and the black dot marking the comet's position in the initial frame, converted to a distance (as in Fig. 2) and divided by the time between the two maps.

3.4. *Velocity Measurements Derived from the Data*

Comet plasma (type I) tail orientation has long been used to estimate the solar wind speed at the location of the comet (Brandt 1968). Far from the comet nucleus ($\sim 10^7$ km), the plasma tail's behavior is determined, for the most part, by the solar wind (Biermann 1951, 1957; Alfvén 1957). When a kink or knot travels down the comet tail, its angular velocity can be determined in the moving coordinate system of Figure 2 (i.e., relative to the moving comet nucleus placed at the origin of coordinates as in Fig. 3) by simply measuring the increasing angle between the nucleus and the feature. The equivalent measurements from Figure 4 yield a perspective-corrected velocity. To translate these measured velocities to an actual solar wind velocity component, corrections are needed for the comet nucleus motion and, in the case of angular velocity, also for the viewing perspective angle. However, the comet tails do not always contain easily recognized moving features such as kinks and knots which can be followed and measured as they move down the tail.

We here introduce an alternative method for determining outward motion that does not require an easily recognizable moving feature. Consider a series of Sun-centered fisheye sky maps such as shown in Figure 1. A radial line away from the Sun defines the direction of a purely radial solar wind outflow. Hence, if we draw a straight line from the Sun to the location of the comet's nucleus in a specific frame (i.e., at a specific time) this defines the instantaneous, purely radial outward flow direction at that location of the comet. In subsequent frames (i.e., at later times), the intersection of this fixed line with the comet tail moves down the tail away from the Sun. We presume that at these distances from the comet nucleus and the Sun, the plasma in the tail has assumed the local speed of the solar wind, and that this intersection moves outward at that speed. When corrected for perspective as described in § 3.2, this speed provides a measure of the solar wind radial velocity component. For each successive frame in the time series, a similar reference radial line is drawn from the Sun to the comet nucleus, and its intersection with the comet tail is tracked through subsequent frames. These lines are tracked not just near the comet nucleus,

TABLE 1
A Selection of Events for Comets NEAT and LINEAR, for Some Features Having the Most Obvious Disruptions

Date First Visible 2004 (UT)	Date Last Visible 2004 (UT)	Radial Velocity (km s^{-1})	Comments
		C/2001 Q4 (NEAT)	
26 Apr 01:28	26 Apr 18:24	349–463	Onset obscured by frame overlap in southern hemisphere, similar to the LINEAR 2004 May 13 event.
28 Apr 21:12	30 Apr 02:00	See Fig. 7	Onset obscured by perspective and noise.
30 Apr 18:56	1 May 16:56	See Fig. 7	Radial velocity gradient.
5 May 02:13	6 May 12:05	See Fig. 6	Radial velocity gradient; also see Kuchar et al. (2006, 2007).
13 May 08:20	19 May 03:29	See Fig. 8	Multiple velocity gradients, including large low-velocity and four smaller high-velocity regions.
19 May 03:29	20 May 15:03	Higher speed > 400	Wavelike disturbance, probably a large off-radial component.
		C/2002 T7 (LINEAR)	
25 Apr 15:01	27 Apr 11:20	320	Small wave and knot.
29 Apr 10:45	30 Apr 02:08	470	Multiple waves.
5 May 12:23	8 May 08:07	See Fig. 7	Knot mostly visible from 2004 May 6 12:05 UT until end.
9 May 21:22	10 May 12:36	416	Large wave (presumably a helical or perspective effect).
13 May 03:15	15 May 02:40	360 to 430	Onset obscured by perspective, measurement extends from middle to end of event, and returns to an ambient wind radial velocity. Appears helical as previous, and further disturbance follows.
17 May 08:51	20 May 09:40	See Fig. 7	Multiple radial velocity gradients measured, ideal perspective.

but at many points down the tail, thus providing a grid of in situ velocities at the crossing points along each radial. Figure 5 illustrates the method for four frames from one of the tail disruptions observed for comet NEAT.

The NEAT and LINEAR comet movies were inspected for changes/disruptions of the comet tails that could be followed down the comet tails, spanning at least five SMEI 102 minute orbits. Table 1 lists 12 time periods or ''events'' associated with comet-tail motion which can be measured with the above technique, giving the times when the feature first appeared and disappeared; in some cases, a range of velocities and a morphological description are given. Some of the resulting velocities are also presented in graphic form in Figures 6, 7, and 8. Figure 6 shows a sequence for NEAT covering the time period starting 2004 May 4 at 19:27 UT, through May 6 12:05 UT. Contours of radial velocity are presented as a function of distance the comet has traversed versus distance, x, down the comet tail, as illustrated in Figure 2. The locations of actual data points are shown,

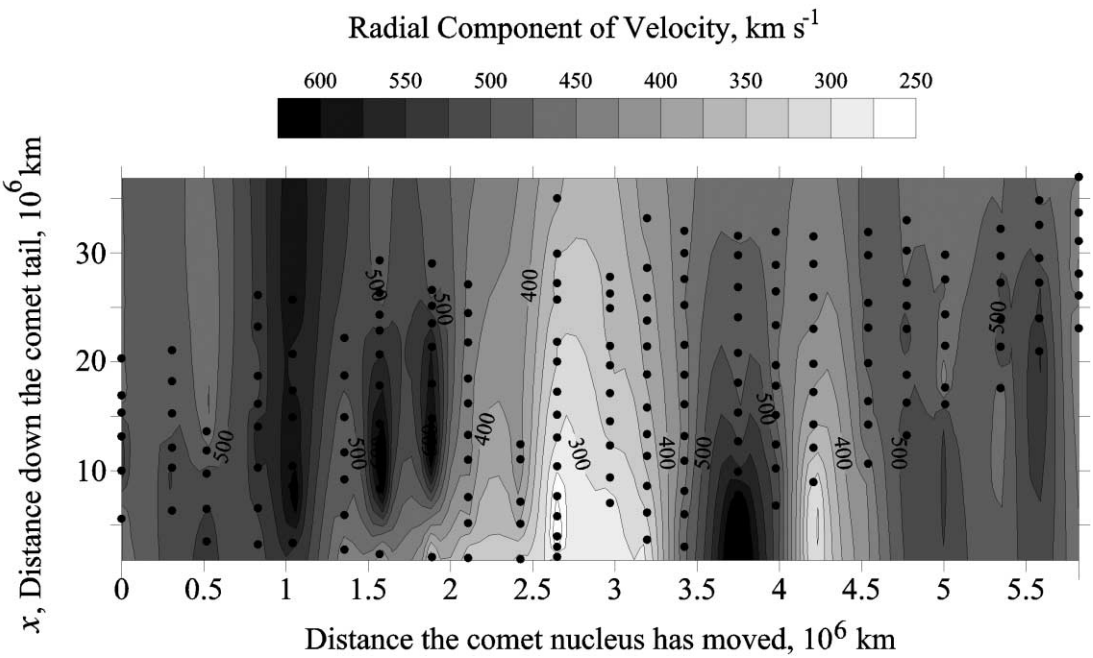

Fig. 6.— Plot of radial velocity observed for comet NEAT, with data starting 02:13 UT on 2004 May 4. Each data point uses a pair of SMEI sky maps, and each vertical column of dots represents a series of measurements along a radial, as illustrated in Fig. 5. The horizontal location of a data point is the orbital plane distance the comet has moved relative to the above arbitrary beginning time, for the earlier of the pair of maps. Radial velocity is the distance x divided by the elapsed time between the pair of maps. The data points illustrated are expanded into a complete contour map by a kriging process. The resulting contour map is a display of solar wind radial velocity in the comet's orbital plane extending outward by up to 0.25 AU from the comet's orbit.

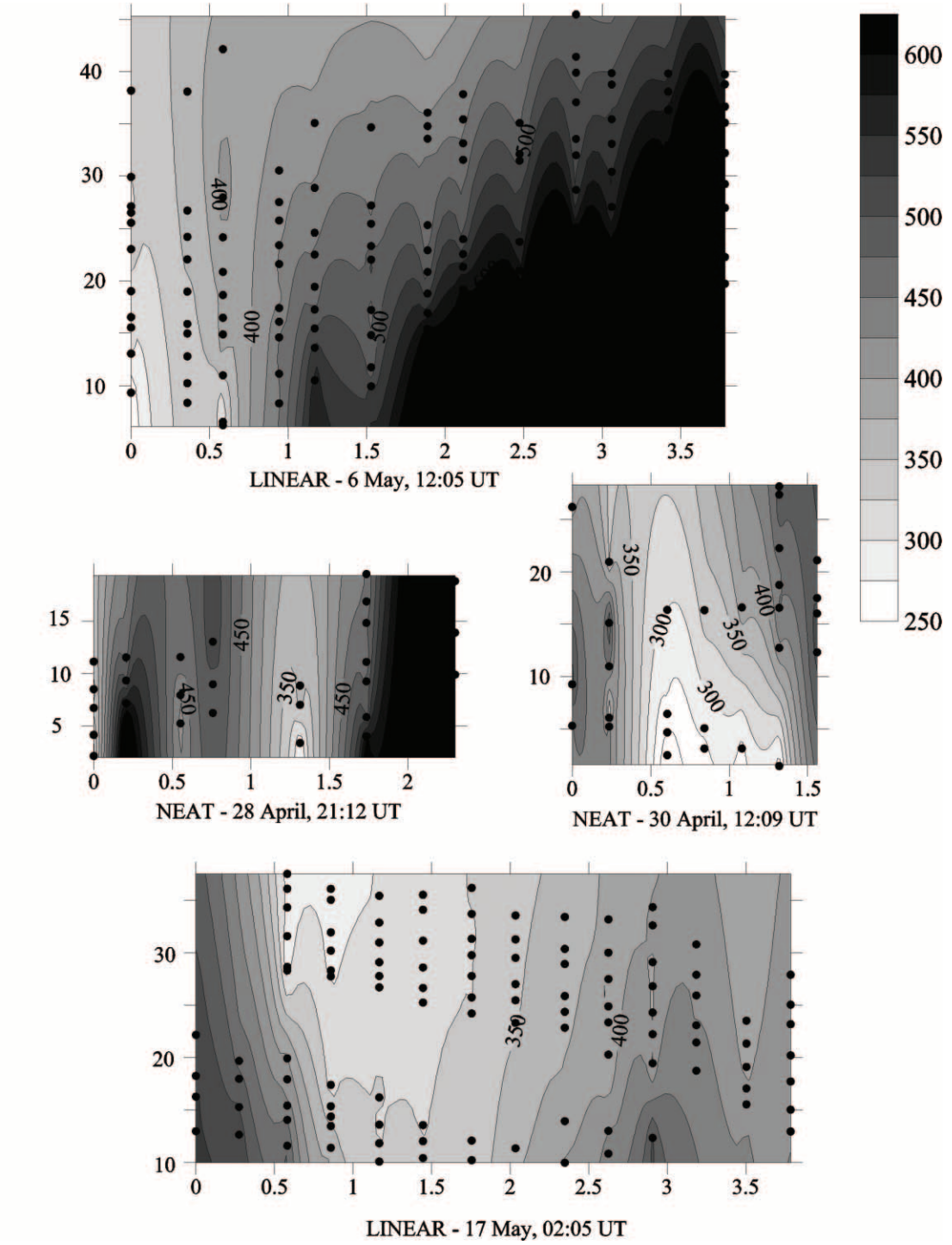

FIG. 7.—Additional time periods from Table 1. These show that these comets frequently encounter regions of slower solar wind, and that such regions are often $\sim 10^6$ km in size. Axes and scales are the same as in Fig. 6.

and a regular grid for the plot was filled in by the method of "kriging." Figures 7 and 8 present similar plots for some different selections from Table 1. The columns of data points in Figures 6 and 7 locate the measurements from subsequent SMEI orbits, mapped to the predetermined nucleus position defined by the first frame in the sequence.

This method of measurement automatically takes into account the comet's orbital motion relative to the stationary Sun-Earth line. The small motion of Earth relative to this line is here considered to have negligible impact on the radial velocity measurements using this method. Possible solar wind nonradial velocity components can exist, but these were virtually undetectable in all but one of the events. Even here, this had an insignificant impact on our radial component velocity measurements. The two methods of measuring radial velocity agreed in several cases where an easily tracked feature moving down the comet tail was available.

3.5. *Interplanetary Scintillation*

Interplanetary scintillation (IPS) is the variation in apparent intensity at meter wavelengths from compact radio sources ("point sources") produced by density inhomogeneities in the

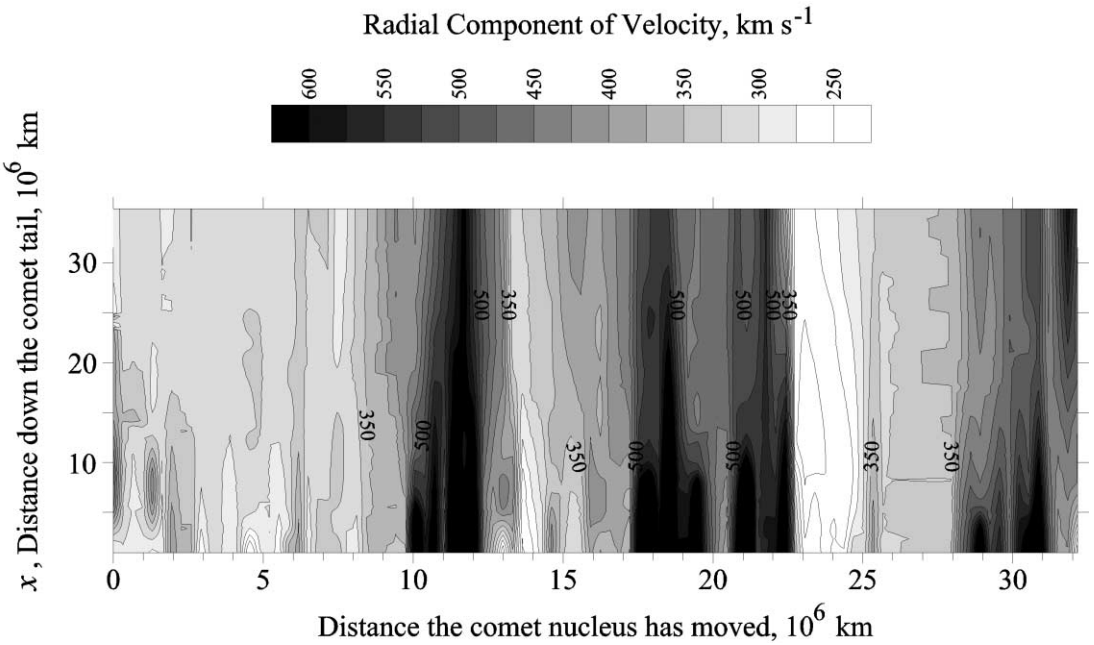

FIG. 8.— Similar to Figs. 6 and 7, but for comet NEAT starting 2004 May 9 at 16:17 UT and including about 10 days of data. Because of the much longer time span, the horizontal scale here is compressed fivefold relative to that of the other figures, and the locations of the densely spaced individual data points are suppressed. SMEI had a data gap between 26 and 28×10^6 km along the horizontal axis. The larger time span here includes passage of the comet through at least three, if not several more, regions of higher solar wind radial velocity, as well as a lower velocity region starting at 23×10^6 km following these.

solar wind. This produces a drifting pattern of scintillation across the Earth and thus allows IPS to be used as a probe for investigating the inner heliosphere. Such data have been used to measure small-scale (~150 km) heliospheric density variations along the line of sight. These have been investigated for over 40 years by employing various methods of interpretation and analyses (e.g., Houminer 1971; Hewish & Bravo 1986; Behannon et al. 1991; Coles 1996; Breen et al. 1996; Bisi et al. 2005; Jackson & Hick 2005; Jackson et al. 2007a; Bisi et al. 2007a). In this paper, data from the Solar Terrestrial Environment Laboratory (STELab) IPS arrays in Japan were used to reconstruct 3D density and velocity structure of the inner heliosphere (Jackson et al. 1998, 2003; Jackson & Hick 2005). In addition, data from the Wilcox Solar Observatory (WSO) were incorporated into the IPS reconstructions to yield the heliospheric magnetic-field distributions through use of the Stanford Current-Sheet Source-Surface (CSSS) model (e.g., Dunn et al. 2005).

3.6. *Three-dimensional Reconstructions from IPS Data*

At present, our 3D reconstruction incorporates a purely kinematic solar wind model. Given the velocity and density of an inner boundary (the "source surface"), a fully 3D model best fitting the observations is iteratively calculated. It assumes a purely radial outflow and enforces conservation of mass and mass flux (e.g., Jackson et al. 1998; Jackson & Hick 2005). If the line-of-sight integrations of 3D solar wind at large solar distances do not match the overall observations, then the source surface values are iteratively modified to reduce the differences. This technique has been used to analyze CME-associated structures using IPS, such as those of the Bastille Day CME of 2000 July 14 (e.g., Jackson et al. 2003), and SMEI Thomson scattering observations (Jackson et al. 2006, 2007b; Bisi et al. 2007b, 2008).

The time series of 3D density, velocity, and magnetic field resulting from the IPS reconstructions are used to evaluate these quantities versus time at Earth, or at the comet nucleus locations. These latter in turn can be compared with periods of activity in the comet tails.

3.7. *ACE Measurements*

The solar wind in situ measurements from the *Advanced Composition Explorer* (*ACE*; Stone et al. 1998) spacecraft have long been used to provide "ground truth" verification to the IPS/SMEI 3D reconstructions (e.g., Jackson et al. 2003). *ACE* is located at the first Lagrange point L1, and is thus about 0.01 AU away from Earth toward the Sun. Large-scale features observed by the above IPS reconstructions are, in most cases, confirmed by the in situ measurements (Jackson et al. 1998, 2003; Jackson & Hick 2005). Confirmation of smaller scale features, such as those of small amplitude or lasting less than a day, is less frequent. This latter is likely due to the limited number of lines of sight provided by the IPS arrays, so that small features are either missed in the observation or are unresolved in the 3D reconstructions.

4. RESULTS

The present work is a further analysis of the tail motions of the two comets using SMEI data that was reported earlier (Kuchar et al. 2006, 2007). Here we present significantly more examples of comet-tail motion. In addition, to better ascertain solar wind/comet-tail radial velocity values, we convert the SMEI sky maps showing angular positions on the sky to maps showing approximate linear distance along the comet tail.

In all but two of the selected "events" in Table 1 (comet NEAT starting 13 May and shown in Figure 8 for a longer time period, and again comet NEAT starting 19 May), the radial component of solar wind velocity drops during the perturbation, typically by ~100 km s^{-1}, and then returns to a higher value. This provides an explanation for the changing appearance with time mentioned in § 3.3, at least for these particular events as they propagate down the comet tail. During the transition to the lower velocity,

TABLE 2
Summary of IPS 3D Reconstruction Data, Time within ±12 and ±6 hr at Each Comet

Date (2004)	Orbit Time (UT)	No. IPS Signatures at Disturbance	Disturbance Morphology[a]
Comet NEAT (C2001/Q4): 9 events, time within ±12 hr			
Apr 25	22:05:47	1	v
Apr 29	20:55:20	2	n, v
May 05	00:32:03	1	n
May 10	04:08:46	2	n, v
May 11	02:09:33	3	v, B_r, B_t
May 12	13:43:08	3	v, B_r, B_t
May 13	13:25:31	2	B_r, B_t (both cross 0)
May 15	06:03:53	4	n, v, B_r, B_t
May 18	08:34:14	2	n, v
Comet LINEAR (C2002/T7): 7 events, time within ±12 hr			
Apr 25	17:00:59	3	n, B_r, B_t
Apr 29	10:45:44	1	v
May 05	02:13:39	4	n, v, B_r, B_t
May 09	23:03:58	2	n, v
May 13	04:57:31	2	n, v
May 17	08:51:51	4	n, v, B_r, B_t
May 26	02:50:05	4	n, v, B_r, B_t
Comet NEAT (C2001/Q4): 9 events, time within ±6 hr			
Apr 25	22:05:47	1	v
Apr 29	20:55:20	2	n, v
May 05	00:32:03	1	N
May 10	04:08:46	2	n, v
May 11	02:09:33	3	v, B_r, B_t
May 12	13:43:08	2	v, B_r
May 13	13:25:31	0	NS
May 15	06:03:53	3	n, v, B_r
May 18	08:34:14	2	n, v
Comet LINEAR (C2002/T7): 7 events, time within ±6 hr			
Apr 25	17:00:59	2	B_r, B_t
Apr 29	10:45:44	1	v
May 05	02:13:39	4	n, v, B_r, B_t
May 09	23:03:58	2	n, v
May 13	04:57:31	2	n, v
May 17	08:51:51	4	n, v, B_r, B_t
May 26	02:50:05	3	n, B_r, B_t

Notes.—Last two columns show the number and type (disturbance morphology) of IPS signatures seen at the time of the disturbance.

[a] NS = none of the above signatures seen in the IPS data; n = electron density of the solar wind (number of e^- cm^{-3}); v = solar wind radial velocity (km s^{-1}); B_r = change in solar wind radial component of magnetic field; B_t = change in solar wind tangential component of magnetic field.

the comet-tail outward radial motion decreases and the aberration increases. The events measured here can be compared/contrasted to a "disconnection event" recently viewed close to the Sun and discussed in Vourlidas et al. (2007).

We also examined 3D reconstructions of the inner heliosphere in density, velocity, and magnetic field using IPS and WSO data. Events were selected from Table 1 for those cases where an unambiguous time could be discerned at which the disturbance passed the location of the comet nucleus. The reconstructions were then examined at that location and time for changes in density, velocity, or magnetic field. An additional LINEAR event (26 May) was included for which the data were insufficient for a direct radial velocity measurement, due to the Sun-facing camera's shutter being closed and obscuring the view of the comet. Table 2 lists IPS signatures evaluated at the comet nucleus and coinciding within both ±12 hr of the SMEI comet-tail disruption onset times and with a more stringent ±6 hr. The inner heliosphere is sufficiently active at this time so that something among the density, velocity, or magnetic field listed in Table 2 is seen to be changing within the indicated time for most of the events listed in the Table. However, no consistent correlation with a particular quantity emerges from Table 2's list of signatures.

Similarly, no consistent correlation was found when data from *ACE* were examined for density, velocity, and/or magnetic-field changes occurring close in time to the comet-tail events listed here. Finally, as we concluded with earlier work (Kuchar et al. 2007), only a fraction of these events lie close enough to the HCS for this to be a possible cause of the comet-tail motion discussed here.

5. SUMMARY AND CONCLUSIONS

We could not establish any clear correlation between comet-tail motions and variations in *ACE* or in the IPS 3D reconstructions. The IPS 3D reconstructions have resolutions of approximately $20^\circ \times 20^\circ$ in latitude and longitude and times of about one day. No corresponding patterns of change with time in these reconstructions coincide with the times of the comet-tail events. Similarly, even for the nearest of comet-tail events, *ACE* remains more than 20° away from the comet nucleus radial. The simplest explanation for not finding any correlation between these data sets is that the scale sizes of the solar wind perturbations causing these comet-tail motions are sufficiently small that in effect *ACE* was measuring a different part of the solar wind, and the angular resolution of the 3D reconstructions is too coarse presently to resolve them.

A kink has typically moved 0.05–0.10 AU down the comet tail when it assumes its characteristic angular size as viewed from the Sun. Beyond this, the angular size grows slowly, if at all. Often, individual knots of material can be discerned within the kink, not necessarily flowing along a radial from the Sun, but still measurable over several or many SMEI 102 minute orbits. For these, some nonradial motion within the solar wind is required, but in all cases but one (see § 3.4) the nonradial component of velocity is negligible compared to the radial velocity itself.

These observations of tail motion are near 1 AU, and make the assumption that changes in solar wind speed are rendered visible by changes in radially outward comet-tail motion as the comets move through the sky. Here, abrupt changes in this outward motion are often observed in transitions through regions of lower-than-ambient solar wind velocity, typically 50–100 km s^{-1}. In the transverse direction, the size of the regions of changed and often reduced radial velocity are of the order of $0.5–1.0 \times 10^6$ km. The measurement technique introduced here measures regions of fast and slow solar wind radial velocity equally well. However, the "kink" appearance of the tail that so easily distinguishes the large disruptions is caused simply by the later, faster region of solar wind catching up with the transient slower portion, initiating the majority of the "events" highlighted here.

These observations are consistent with a flux-tube description of the solar wind (Borovsky 2006). In this case, a passing distribution of plasma discontinuities observed in situ with spacecraft such as *ACE* is viewed as a multitude of separate flux tubes, each containing its own plasma, and with tube size of order 5×10^5 km. Furthermore, tubes having lower velocity solar wind tend to be larger (Borovsky 2006, 2007), which is consistent with our

analysis of these outward comet-tail motions. Thus, as the comet tail spreads out into the solar wind, its appearance would typically be determined by an average of several flux tubes or more, but in the case of lower velocity, a single flux tube would become dominant.

We thank Asoka Mendis and Karen R. Flammer for numerous useful discussions and Kim Griest for a critical reading of the manuscript. The authors acknowledge and thank the group at STELab, Nagoya University, Japan (M. Kojima, M. Tokumaru, K. Fujiki, and students), for their continued support and for making the IPS data available under the auspices of a joint collaborative agreement between the Center for Astrophysics and Space Sciences (CASS), UCSD, and STELab. The authors also wish to thank the *ACE*/SWEPAM and *ACE*/MAG groups for use of the solar wind proton density, velocity and magnetic field measurements used in this paper for in situ comparisons, and the Wilcox Solar Observatory for providing magnetic field source-surface data. SMEI was designed and constructed by a team of scientists and engineers from the US Air Force Research Laboratory, the University of California at San Diego, Boston College, Boston University, and the University of Birmingham in the UK. Financial support was provided by the Air Force, the University of Birmingham, and NASA. The present work was supported in part by grants NSF ATM0331513 and NASA NNG05GM58G.

REFERENCES

Alfvén, H. 1957, Tellus, 9, 92
Behannon, K. W., Burlaga, L. F., & Hewish, A. 1991, J. Geophys. Res., 96, 21213
Biermann, L. 1951, Zh. Fiz. Astrophys., 29, 274
———. 1957, Observatory, 77, 109
Bisi, M. M., Breen, A. R., Fallows, R. A., Thomasson, P., Jones, R. A., & Wannberg, G. 2005, in Solar Wind 11/SOHO 16, Connecting Sun and Heliosphere (ESA SP-592; Garching: ESA), 593
Bisi, M. M., Fallows, R. A. Breen, A. R., Habbal, S. R., & Jones, R. A. 2007a, J. Geophys. Res., 112, A06101, DOI: 10.1029/2006JA012166
Bisi, M. M., Jackson, B. V., Hick, P. P., Buffington, A., & Clover, J. M. 2008, Geophys. Res., submitted
———. 2007b, in Proc. 4th Asia-Oceania Geophysical Society General Assembly, Advances in Geosciences, submitted
Borovsky, J. E. 2006, Phys. Plasmas, 13, 056505
———. 2007, J. Geophys. Res., submitted
Brandt, J. C. 1968, ARA&A, 6, 267
Brandt, J. C., & Chapman, R. D. 2004, Introduction to Comets (2nd Ed.; Cambridge: Cambridge Univ. Press)
Brandt, J. C., & Snow, M. 2000, Icarus, 148, 52
Breen, A. R., Coles, W. A., Grall, R. R., Klinglesmith, M. T., Markkanen, J., Moran, P. J., Tegid, B., & Williams, P. J. S. 1996, Ann. Geophys., 14, 1235
Buffington, A., Band, D. L., Jackson, B. V., Hick, P. P., & Smith, A. C. 2006, ApJ, 637, 880
Buffington, A., Morrill, J. S., Hick, P. P., Howard, R. A., Jackson, B. V., & Webb, D. F. 2007, Proc. SPIE, 6689, 66890B-1
Coles, W. A. 1996, Ap&SS, 243, 87
Cox, A. N., ed. 2000, Allen's Astrophysical Quantities (4th Ed.; New York: Springer)
Dunn, T., Jackson, B. V., Hick, P. P., Buffington, A., & Zhao, X. P. 2005, Sol. Phys., 227, 339
Eyles, C. J., et al. 2003, Sol. Phys., 217, 319
Hewish, A., & Bravo, S. 1986, Sol. Phys., 106, 185
Hick, P. P., Buffington, A., & Jackson, B. V. 2005, Proc SPIE, 5901, 59011C-1
———. 2007, Proc. SPIE, 6689, 66890C-1
Houminer, Z. 1971, Nature Phys. Sci., 231, 165
Jackson, B. V., Boyer, J. A., Hick, P. P., Buffington, A., Bisi, M. M., & Crider, D. H. 2007a, Sol. Phys., 241, 385
Jackson, B. V., Buffington, A., Hick, P. P., Bisi, M. M., & Jensen, E. A. 2007b, Proc. SPIE, 6689, 66890G-1
Jackson, B. V., Buffington, A., Hick, P. P., Wang, X., & Webb, D. 2006, J. Geophys. Res., 111, A04S91, DOI: 10.1029/2004JA0109432
Jackson, B. V., & Hick, P. P. 2005, in Solar and Space Weather Radiophysics, Current Status and Future Developments, ed. D. E. Gary, & C. U. Keller (Dordrecht: Kluwer), 355
Jackson, B. V., Hick, P. L., Kojima, M., & Yokobe, A. 1998, J. Geophys. Res., 103, 12049
Jackson, B. V., et al. 2003, in AIP Conf. Proc. 679, Solar Wind Ten (Woodbury: AIP), 75
———. 2004, Sol. Phys., 225, 177
Kuchar, T. A., Buffington, A., Howard, T. A., Arge, C. N., Hick, P. P., Jackson, B. V., & Webb, D. F. 2006, EOS Trans. AGU, 87 (52), Fall Meet. Suppl., Abstr. SH32A-08
Kuchar, T. A., et al. 2007, J. Geophys. Res., in press
Mendis, D. A. 2006, Geophys. Monogr., 167, 31
Mizuno, D. R., et al. 2005, J. Geophys. Res., 110(A7), A07230, DOI: 10.1029/2004JA010689
Niedner, M. B. Jr., & Brandt, J. C. 1978, ApJ, 223, 655
Stone, E. C., Frandsen, A. M., Mewaldt, R. A., Christian, E. R., Margolies, D., Ormes, J. F., & Snow, F. 1998, Space Sci. Rev., 86, 1, DOI: 10.1023/A:1005082526237
Vourlidas, A., Davis, C. J., Eyles, C. J., Crothers, S. R., Harrison, R. A., Howard, R. A., Moses, J. D., & Socker, D. G. 2007, ApJ, 668, L79